

## Article

# Eigen-Sensitivity-Based Sliding Mode Control for LFO Damping in DFIG-Integrated Power Systems

Rui Zhang <sup>1</sup>, Hao Zhang <sup>2</sup>, Jianqiao Ye <sup>3,\*</sup>, Jiaqing Wang <sup>1</sup>, Qing Liu <sup>1</sup> and Shenghu Li <sup>3</sup>

<sup>1</sup> State Grid Anhui Electric Power Co., Ltd., Hefei 230009, China; zhangrui18757@163.com (R.Z.); wangjqah@163.com (J.W.); tsingleo@126.com (Q.L.)

<sup>2</sup> State Grid Hefei Electric Power Supply Company, Hefei 230009, China; m18326178536\_1@163.com

<sup>3</sup> School of Electrical Engineering and Automation, Hefei University of Technology, Hefei 230009, China; shenghuli@hfut.edu.cn

\* Correspondence: jianqiao\_ye1122@mail.hfut.edu.cn

**Abstract:** Low-frequency oscillation (LFO) of the synchronous generators in power systems by wind power is boring. To improve the robustness of the damping control scheme, this paper applies the sliding mode control (SMC) at the doubly fed induction generator (DFIG), with the parameter of the SMC optimized by the eigen-sensitivity. The originalities lie in, (1) the states strongly associated with the critical modes are newly applied to design the sliding surface, (2) the closed-loop model of the power system with the improved equivalent control is derived to analyze the damping effect on the critical modes and the undesirable effect on the noncritical modes, (3) the gain in the improved equivalent control is optimized to damp the critical and noncritical modes, and (4) the eigenvector sensitivity is improved to derive the second-order eigen-sensitivity to solve the nonlinear optimization. Numerical results show that the proposed model damps the critical modes effectively for different wind speeds, while the undesirable effect on the noncritical modes is avoided.

**Keywords:** doubly fed induction generator (DFIG); eigen-sensitivity; low-frequency oscillation (LFO); optimization; power system control; sliding mode control (SMC)



**Citation:** Zhang, R.; Zhang, H.; Ye, J.; Wang, J.; Liu, Q.; Li, S.

Eigen-Sensitivity-Based Sliding Mode Control for LFO Damping in DFIG-Integrated Power Systems. *Energies* **2023**, *16*, 4256. <https://doi.org/10.3390/en16104256>

Academic Editor: Abu-Siada Ahmed

Received: 26 April 2023

Revised: 17 May 2023

Accepted: 20 May 2023

Published: 22 May 2023



**Copyright:** © 2023 by the authors. Licensee MDPI, Basel, Switzerland. This article is an open access article distributed under the terms and conditions of the Creative Commons Attribution (CC BY) license (<https://creativecommons.org/licenses/by/4.0/>).

## 1. Introduction

### 1.1. Background of This Paper

With the increase in smart grids [1,2] and new energy sources (e.g., wind power), the problems of power system reliability have attracted extensive attention from scholars. Power system reliability is classified by the adequacy and security. The adequacy shows the ability of power systems to supply the load for consumers during the steady-state operation. The evaluation indices include LOLP, EPNS, EDNS, LOLD, etc., [3,4].

The security shows the ability of power systems to keep synchronism, without losing angular stability, frequency stability, voltage stability, and poorly damped oscillation modes during the dynamic process. The indices include the stability margin, the damping ratio, the oscillation frequency, etc., [5]. The doubly fed induction generators (DFIGs) affect the power output of the synchronous generator (SG) and the oscillation characteristics of power systems [6]. The weakly damped low-frequency oscillation (LFO) of the mechanical transient of the SGs may undesirably trip the SGs and the backup relays [7].

The LFOs are often damped by the power system stabilizer (PSS) installed at the exciter of the SGs. The parameters of the PSS are tuned by the damping torque analysis based on small signal analysis and validated by the dynamic simulation after a large disturbance [8–11]. With more and more SGs being replaced by wind power, the power oscillation damper (POD) installed at the DFIG has attracted the interest of researchers [12,13]. Since the power balance of a system is maintained by the SGs and DFIGs, the power control to the DFIGs affects the SGs' transient [14,15]. The POD has a similar structure as the PSS [16,17], which is expected to have a similar control effect.

However, the configuration and control strategy of the DFIG are different from those of the SG, whose mechanical input is uncertain due to the wind speeds. A robust design for the POD is challenging.

Power system stability control may be implemented with the transfer function or the state space model. The former can deal with the nonlinear element but is difficult for systems with a large dimension. The latter can treat large systems but is based on linearization to the equilibrium point. Its controllable range may be limited under the changing operating conditions.

The motivation of this paper is to consider the effect of ensuring the performance of POD operation under different operating conditions. The sliding mode control (SMC) enforces the states to a desirable sliding surface with a robust performance. To tune its parameters, the system scale in existing studies is often small and not suitable for power systems. Hence, this paper tries to apply the SMC to the POD at the DFIG to damp the LFO mode, with the control parameters optimized by the eigen-sensitivities.

### 1.2. Literature Review and Comparison

The LFO in a power system is suppressed by intelligent algorithms to optimize the parameters of the device. The gravitational search algorithm [18], imperialist competitive algorithm [19], bacterial foraging optimization algorithm [20], and bacterial swarm optimization [21] are studied in a power system. The design methods for the PSS (POD) include the damping torque analysis, the modal analysis, etc. Using damping torque analysis, the control effect of the PSS is decided by the gain and lead-lag parameters. Based on the phasor relation of damping and electromagnetic torques, the compensation angle is found to tune the parameters [22]. A frequency controller is designed [23] to ascertain the required damping torque [24]. The damping torque analysis often focuses on the local SG. Coordination among multi-PSS with dynamic interaction is needed [25].

The oscillation frequency and the damping ratio are derived from the modal analysis. The control parameters are gradually changed to draw the locus of the LFO modes to verify the control effect. It is computationally expensive since each time only one parameter is checked [26]. Sensitivities of eigenvalues are more effective to decide the control effect [27]. For the DFIG-integrated system, the accuracy of the eigen-sensitivity is related to the interface equation and voltage dynamic [28]. Inaccurate modeling yields wrong judgments regarding the system's stability and control settings.

The above methods are based on linearization to a given operation point; hence, the control setting may be not effective for other states or contingencies. To improve the robustness, fuzzy logic and adaptive control may be used [29,30], whose feasibility for large systems is to be further validated. As a nonlinear control, the SMC with the sliding surface selected and the control law design [31] enforces the system states to the sliding surface in a finite time, tolerates the disturbance, and has a fast response [32], which may be used to damp the LFO in power systems. With the rotor speeds of the SGs selected as the sliding surface, the SMC-based PSS at the SG [33] and the SMC for the DFIG are designed for the LFO damping [34]. A drawback is selecting the sliding surface for systems with many SGs. In [35], the optimal sliding surface is designed to exploit the advantages of the SMC, but the derivation with the state matrix is complex.

The time derivative of the sliding surface is derived to find the relative degree of the SMC and design the switch control. The latter with the signum function switches between two structures to drive the states toward the sliding surface [36] and enhances robustness against uncertainties. In [37], the SMC is applied to the load frequency control for a multi-area system, insensitive to the disturbances. Chattering of the SMC may be avoided with the second-order model, e.g., the twisting algorithm, the super-twisting algorithm, the drift algorithm, etc., [38].

To enhance the damping, the equivalent control is applied to the SMC, which accelerates the states reaching the sliding surface [39]. Ref. [40] derives the small signal model to study the sliding mode dynamics with the eigenvalues. In [41,42], the equivalent

control is designed based on the linear matrix inequality and the Lyapunov function, which provide stable eigenvalues. The gain in the SMC is optimized with the pole placement and linear quadratic regulator in [43,44], where the eigenvalue bound is set for parametric uncertainties. However, these methods are difficult to solve for a large power system [45]. A reduction in the system's configuration and control is needed.

The control parameter may be optimized with heuristic or direct optimization methods. The particle swarm optimization and firefly algorithm [46,47] are computationally expensive, and cannot prove global optimality. The interior point method [48] is straightforward and has good convergence, but it needs the derivation of Jacobian/Hessen matrices. Due to the nonlinearity of power systems, the first-order eigenvalue sensitivity has the truncation error and may be reduced with the second-order one [49,50]. The above eigen-sensitivities may be derived with a parameter perturbation or normalization condition [51–53]. The former has a low calculation efficiency. The latter has a strong assumption for the practical system. Hence, the analytical expression of the first- and the second-order eigen-sensitivities is the basis of the parameter optimization for the SMC.

### 1.3. Contribution of This Paper

To improve the robustness of the damping control scheme, this paper applies the sliding mode control (SMC) at the doubly fed induction generator (DFIG), with the parameter of the SMC optimized by the eigen-sensitivity. The originalities lie in, (1) the states strongly associated with the critical modes are newly applied to design the sliding surface, (2) the closed-loop model of the power system with the improved equivalent control is derived to analyze the damping effect on the critical modes and the undesirable effect on the noncritical modes, (3) the gain of the improved equivalent control is optimized to damp the critical and the noncritical modes, and (4) the eigenvector sensitivity is improved to derive the second-order eigen-sensitivity to solve the nonlinear optimization.

### 1.4. Layout of This Paper

In Section 2, the small-disturbance model of the wind power system with the DFIG is given as the basis for the following control design. In Section 3, the sliding surface is selected by the critical states. The improved equivalent control is applied to the SMC. In Section 4, the optimization model based on the eigen-sensitivity is proposed to adjust the gain to damp the critical and noncritical modes. In Section 5, the simulation result is given to verify the control effect of the proposed SMC model. In Section 6, some brief conclusions are given.

## 2. Model of DFIG-Integrated Power System

As shown in Figure 1, a DFIG includes the wind turbine (WT) with the pitch angle control (PAC), the transfer shaft between the WT and the induction generator (IG), the rotor-side converter (RSC) and the grid-side converters (GSC) connected by the dc capacitor, and the transformer or filter between the GSC and the stator. The DFIGs connect the SGs with the transmission grid (T). With the PI controller, the PAC controls the pitch angle  $\beta$ , maintains the rotor speed  $\omega_t$ , and captures the power  $P_t$  with the WT. Then,  $P_t$  is transmitted to the shaft described by a two-mass model. For decoupled control, the DFIG is orientated by the stator voltage. A two-layer strategy is applied. By regulating the direct/quadrature (d/q) voltages and currents, the RSC regulates the active and reactive powers ( $P_s$  and  $Q_s$ ) at the stator, and the GSC maintains the dc voltage and reactive power of the GSC.

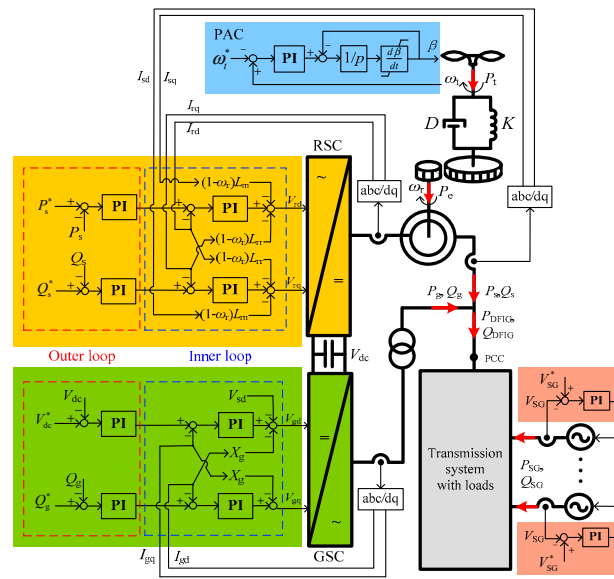


Figure 1. Configuration of DFIG-integrated system.

The SG is described by the motion equation and excitation system. The wind power system with the DFIG is given by [48]

$$\begin{cases} \frac{dx_{SG}}{dt} = f_{SG}(x_{SG}, y_{SG}, y_T) \\ \frac{dx_{DFIG}}{dt} = f_{DFIG}(x_{DFIG}, y_{DFIG}, y_T) \\ 0 = g_{SG}(x_{SG}, y_{SG}, y_T) \\ 0 = g_{DFIG}(x_{DFIG}, y_{DFIG}, y_T) \\ 0 = g_T(y_T) = I - YV \end{cases} \quad (1)$$

where  $f$  and  $g$  denote the differential and algebraic equations,  $x$  and  $y$  are the state and algebraic variables,  $I$ ,  $V$ , and  $Y$  are the current, voltage, and admittance matrix, and  $t$  is the time. The state variables of the DFIG under the maximum power point control include  $\beta$  and its reference  $\beta^*$ , the slip of the WT and the IG ( $s_t, s_r$ ), the torsional angle ( $\gamma$ ), the stator currents  $I_{sd}$  and  $I_{sq}$ , the RSC currents  $I_{rd}$  and  $I_{rq}$  and the references  $I_{rd}^*$  and  $I_{rq}^*$ , the GSC currents  $I_{gd}$  and  $I_{gq}$ , the references  $I_{gd}^*$  and  $I_{gq}^*$ , the voltages of the RSC and GSC ( $V_{rd}, V_{rq}, V_{gd}, V_{gq}$ ), and the dc voltage ( $V_{dc}$ ). The state variables of the SG include the rotor speed of the SG ( $\omega$ ), the power angle ( $\delta$ ), the sub-transient electromotive force ( $E'_q$ ), and the excitation voltage ( $E_f$ ). Note,  $N_{DFIG}$  and  $N_{SG}$  are the numbers of DFIG and SG. Therefore, the dimension of  $x$  is  $N \times 1$ , where  $N = 20 \times N_{DFIG} + 4 \times N_{SG}$ . The dimension of  $y$  is  $M \times 1$ , where  $M = 28 \times N_{DFIG} + 8 \times N_{SG}$ .

### 3. Second-Order SMC Design for LFO Damping

To damp the LFOs, the second-order SMC, including the switch control based on the super-twisting algorithm and the equivalent control based on the eigen-analysis, is designed based on the state equations of the wind power system.

#### 3.1. Sliding Surface Design

By linearizing at the operating point, the state equation of the wind power system is derived [28]

$$\begin{cases} \frac{d\Delta x}{dt} = A\Delta x + B\Delta y \\ 0 = C\Delta x + D\Delta y \end{cases} \quad (2)$$

Then, with the SMC installed at the convertors of the DFIG, the control signal of the SMC ( $u$ ) is introduced, and the state equation is extended to

$$\begin{cases} \frac{d\Delta x}{dt} = A_{N \times N} \Delta x + B_{N \times M} \Delta y + E_{N \times 1} u \\ 0 = C_{M \times N} \Delta x + D_{N \times N} \Delta y + F_{M \times 1} u \end{cases} \tag{3}$$

$$\Rightarrow \frac{d\Delta x}{dt} = (A - BD^{-1}C) \Delta x + (E - BD^{-1}F) u = A_{sys} \Delta x + G_{N \times 1} u$$

where  $A, B, C,$  and  $D$  are the coefficient matrices of the state variable and algebraic variable,  $E, F,$  and  $G$  are the coefficient matrices of  $u$ ,  $A_{sys}$  is the state matrix of the power system with the DFIG, the dimension is  $N \times N$ , and  $\Delta$  denotes the increment.

Equation (3) is solved to obtain many eigenvalues of the power system, in which, the electromechanical oscillation closely associated with the SGs is the most critical to the angular and frequency stability of power systems. The electromechanical modes are the most destabilizing mode of the power system, so it needs to be damped to make it stable. Then, the eigen-analysis is carried out to find the electromechanical mode [28]

$$\begin{cases} A_{sys} v = \lambda v \\ \lambda = \sigma + i\mu \end{cases} \tag{4}$$

$$\begin{cases} 0.1 < f < 2.5 \\ \rho = \left| \frac{\sum_{x_k \in SG, MT} p_k}{1 - \sum_{x_k \in SG, MT} p_k} \right| \gg 1 \end{cases} \tag{5}$$

where  $\lambda$  is the eigenvalue with the real and imaginary parts  $\sigma$  and  $\mu$ ,  $v$  is the right eigenvector, the dimension is  $N \times 1$ ,  $f$  is the frequency,  $\rho$  is the electromechanical loop ratio,  $p$  is the participation factor, and the subscript MT denotes the mechanical transient of the SGs described by the power angle and rotor speed ( $\delta$  and  $\omega$ ).

Among the electromechanical modes, from (6), the critical mode with the lowest damping ratio is found. Where  $\zeta$  is the damping ratio, the superscripts max and min denote the maximum and minimum values.

$$\begin{cases} \sigma < \sigma^{max} \\ \zeta < \zeta^{min} \end{cases} \tag{6}$$

The variables of the critical mode strongly associated ( $\delta$  and  $\omega$ ) are selected to formulate the sliding surface ( $s$ ) in this paper. Since the power angle of the SGs may not recover to the initial value when the fault is cleared,  $s$  is formulated with the rotor speed difference between the SGs, as

$$s_{1 \times 1} = \Delta\omega_{i,j} = \Delta\omega_i - \Delta\omega_j = \varphi_{1 \times N} \Delta x_{N \times 1} = [0 \quad 0 \quad \dots \quad 1 \quad -1 \quad \dots \quad 0] \begin{bmatrix} \Delta x_1 \\ \Delta x_2 \\ \dots \\ \Delta\omega_i \\ \Delta\omega_j \\ \dots \\ \Delta x_N \end{bmatrix} \tag{7}$$

The sliding surface is about the variable of the SGs, while the control signal of the SMC may be considered as the variable of the DFIGs. Since the DFIGs and the SGs are connected through the transmission system, the relation between  $s$  and  $u$  is complex, which is difficult to drive based on a nonlinear model. Hence, the state space model of the power system with the DFIGs is applied to design the SMC. Combining (3) and (7), the first- and the second-order derivatives of  $s$  are derived

$$\frac{\partial s}{\partial t} = \varphi A_{sys} \Delta x + \varphi G u = \varphi A_{sys} \Delta x \tag{8}$$

$$\frac{\partial^2 s}{\partial t^2} = \varphi A_{\text{sys}}^2 \Delta x + \varphi A_{\text{sys}} G u \tag{9}$$

where  $\varphi G = 0$ , and  $\varphi A_{\text{sys}} G \neq 0$ , i.e., the relative degree is 2, and the second-order SMC is required. The conclusion based on the linear model in this paper is the same as that based on the nonlinear model in [31], and by the former, the difficulty in deriving the derivatives of the sliding surface is reduced effectively.

### 3.2. Super-Twisting Algorithm-Based Switch Control Design

In this part, the switch control  $u_{\text{sw}}$  given with the signum function is set, whose value changes adaptively to enforce the states' slide along the sliding surface. Among the algorithms for  $u_{\text{sw}}$ , the super-twisting algorithm reduces chattering, and improves the robustness of the SMC [43], hence it is applied here

$$\begin{cases} u_{\text{sw}} = k_1 u_{\text{sw}1} + k_2 u_{\text{sw}2} \\ \begin{cases} u_{\text{sw}1} = |s|^{\frac{1}{2}} \text{sgn}(s) \\ p u_{\text{sw}2} = \frac{1}{2} \text{sgn}(s) \end{cases} \\ k_1 < 0, k_2 < 0 \end{cases} \tag{10}$$

where  $\text{sgn}(s)$  is given in (11), and  $k_1$  and  $k_2$  are the coefficients controlling the gains of  $u_{\text{sw}1}$  and  $u_{\text{sw}2}$ , respectively.

$$\text{sgn}(s) = \begin{cases} 1, & s > |\varepsilon| \\ \frac{s}{\varepsilon}, & -|\varepsilon| < s < |\varepsilon| \\ -1, & s < -|\varepsilon| \end{cases} \tag{11}$$

To ensure the system reaches the stable state in finite time with the control of the SMC, the coefficients  $k_1$  and  $k_2$  should satisfy the convergence condition [28], where  $M |s|^{1/2}$  imposes the bound of the system's disturbances.

$$\begin{cases} k_1 > 2M \\ k_2 > k_1 \frac{5Mk_1 + 4M^2}{2k_1} \end{cases} \tag{12}$$

### 3.3. Improved Equivalent Control of SMC

To drive the state reaching the sliding surface more quickly, the equivalent control  $u_{\text{eq}}$  is derived by setting  $\partial^2 s / dt^2$  to 0 (13), where  $M_{\text{eq}}$  shows the connection between  $u_{\text{eq}}$  and the system states. The dimension of  $M_{\text{eq}}$  is  $1 \times N$ .

$$\begin{aligned} \frac{\partial^2 s}{\partial t^2} &= \varphi A_{\text{sys}}^2 \Delta x + \varphi A_{\text{sys}} G u_{\text{eq}} = 0 \\ \Rightarrow u_{\text{eq}} &= -(\varphi A_{\text{sys}} G)^{-1} \varphi A_{\text{sys}}^2 \Delta x = M_{\text{eq}} \Delta x \end{aligned} \tag{13}$$

Since  $u_{\text{eq}}$  works on the value of  $\partial^2 s / dt^2$ , which helps to drive  $s$  and  $\partial s / dt$  to 0, the corresponding LFO mode is damped. As shown in Figure 2, the equivalent control adds a feedback path to the RSC, by which, the active power of the DFIG is regulated to damp the LFO modes.

By combining (3) and (13), a closed-loop model is derived

$$\begin{cases} p \Delta x = A_{\text{sys}} \Delta x + G u_{\text{eq}} \\ u_{\text{eq}} = M_{\text{eq}} \Delta x \end{cases} \tag{14}$$

where  $u_{\text{eq}}$  is seen as an algebraic variable, and the state matrix with  $u_{\text{eq}}$  i.e.,  $A_{\text{sys,eq}}$ , is derived in (15), based on which, the LFO modes are found.

$$p \Delta x = (A_{\text{sys}} + G M_{\text{eq}}) \Delta x = A_{\text{sys,eq}} \Delta x \tag{15}$$

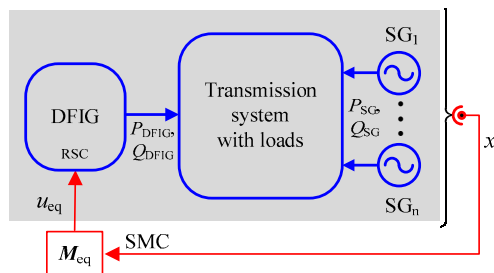


Figure 2. Closed-loop model of power systems with equivalent control.

As shown by the gray area in Figure 3, the marginal values of the damping ratio and the real part of the eigenvalues ( $\zeta_{lim}$  and  $\sigma_{lim}$ ) decide the LFO modes threatening the system’s stability.

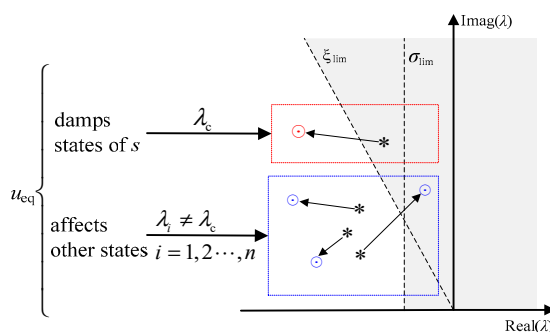


Figure 3. Impact of  $u_{eq}$  on the LFO modes of power systems.

From Figure 3, it can be seen that the improvement in the critical mode ( $\lambda_c$ ) strongly associated with the states of  $s$  quantifies the damping effect of the equivalent control on the LFO. However, for systems with multiple LFO modes,  $u_{eq}$  may affect other LFO modes ( $\lambda_i \neq \lambda_c$ ), reducing the stability level.

To alleviate the undesirable effect, an improved equivalent control  $u_{eq*}$  is proposed with an adjustable gain  $K_{eq}$  (16). By substituting (16) to (14), one obtains (17). It can be seen that  $u_{eq*}$  reduces the value of  $\partial^2 s / dt^2$ . The damping effect improves with the increase in  $K_{eq}$  (not larger than 1), but the undesirable effect may be more obvious.

$$u_{eq*} = K_{eq} M_{eq} \Delta x = K_{eq} u_{eq} \tag{16}$$

$$\left| \frac{\partial^2 s}{\partial t^2} \right| = \left| (1 - K_{eq}) \varphi A_{sys}^2 \Delta x \right| \leq \left| \varphi A_{sys}^2 \Delta x \right| \tag{17}$$

With  $u_{eq*}$ , both the state matrix  $A_{sys,eq*}$ , and the LFO modes are related to  $K_{eq}$  (18), where the subscript 0 denotes the initial value. Hence,  $K_{eq}$  may be tuned to improve the flexibility and the control effect of the SMC, as shown in Section 4.

$$\begin{aligned} \frac{d\Delta x}{dt} &= (A_{sys} + K_{eq} G M_{eq}) \Delta x = A_{sys,eq*} \Delta x \\ \Rightarrow \lambda_i &= \lambda_{i,0} + \Delta \lambda_i(K_{eq}) \end{aligned} \tag{18}$$

The proposed improved SMC is shown in Figure 4. With the SMC, the state space equation of the power system is given by

$$\begin{aligned} \frac{d\Delta x}{dt} &= A_{sys} \Delta x + G u = A_{sys} \Delta x + G (u_{sw} + u_{eq}) \\ &= (A_{sys} + G K_{eq} M_{eq}) \Delta x + G u_{sw} \\ &= A_{sys,eq*} \Delta x + G u_{sw} \end{aligned} \tag{19}$$

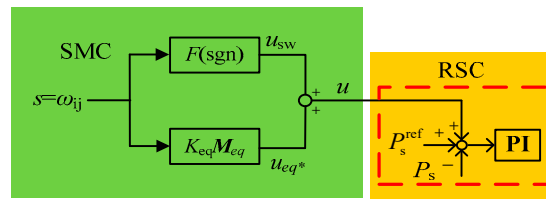


Figure 4. Schematic design of the proposed SMC for the RSC.

#### 4. Optimization to $K_{eq}$ Based on The Second Eigen-Sensitivity

To optimize  $K_{eq}$  to balance the damping effect and undesirable effect of  $u_{eq^*}$ , the linear matrix inequality or Lyapunov function may be applied [44], which is, however, difficult due to the state matrix of a high order. Hence, the second-order eigen-sensitivity model is improved to derive  $K_{eq}$ .

##### 4.1. Optimization Model to $K_{eq}$

The damping effect of  $u_{eq^*}$  is shown with the change in the critical mode; hence, the objective function  $F$  is given by the damping ratio  $\zeta_c$  with the correlation with the eigenvalue  $\lambda_c$ .

$$\begin{aligned}
 F &= \min(-\zeta_c) = \frac{\sigma_c}{(\sigma_c^2 + \mu_c^2)^{1/2}} = \frac{\text{real}(\lambda_c)}{(\text{real}(\lambda_c)^2 + \text{imag}(\lambda_c)^2)^{1/2}} \\
 &= \frac{\text{real}[\lambda_{i,0} + \Delta\lambda_i(K_{eq})]}{(\text{real}[\lambda_{i,0} + \Delta\lambda_i(K_{eq})]^2 + \text{imag}[\lambda_{i,0} + \Delta\lambda_i(K_{eq})]^2)^{1/2}}
 \end{aligned}
 \tag{20}$$

From (14), the correlation is between the eigenvalue  $\lambda_c$  and  $K_{eq}$ . Therefore, the optimal  $K_{eq}$  may be calculated to obtain the minimum result of  $F$ .

To limit the undesirable effect to other LFO modes, the inequality constraints of the real part and the damping ratio are included in (21). The bound of  $K_{eq}$  is given in (22).

$$g_1 : \begin{cases} \sigma_i \leq \sigma_{lim} \\ \zeta_i \geq \zeta_{lim} \end{cases}
 \tag{21}$$

$$g_2 : 0 \leq K_{eq} \leq 1
 \tag{22}$$

The optimization model may be solved by a heuristic method or direct solution. The former is easy to implement, but it is time-consuming, and cannot guarantee global optimization. The latter, e.g., the interior point method, is straightforward, and has the advantage of fast convergence. Based on the latter,  $F$  is augmented to the Lagrange function  $L$  with the Lagrange multipliers  $q^T$  and  $o^T$  (23), where the inequality constraints are changed to the equality constraints with the slack variables ( $\kappa$  and  $l$ ). The optimal solution is obtained when the derivatives of  $L$  with respect to all the variables and Lagrange multipliers are 0, which is derived with the Newton iteration.

$$\begin{cases} L = F - q^T (g_{1,2} - l - g_{1,2}^{\min}) \\ \quad + o^T (g_{1,2} + u - g_{1,2}^{\max}) - q^T l - o^T \kappa \\ g_{1,2} + u - g_{1,2}^{\max} = 0 \\ g_{1,2} - l - g_{1,2}^{\min} = 0 \end{cases}
 \tag{23}$$

4.2. The First- and Second-Order Eigen-Sensitivities

The difficulty of solving (23) is to find the derivatives of  $\lambda_i$  and  $\xi_i$  with respect to  $K_{eq}$ , and form the Jacobian and Hessian matrices for the optimization. Hence, the eigen-sensitivity is to be derived. The first-order eigen-sensitivity is quite common

$$\frac{\partial \lambda_i}{\partial K_{eq}} = w^T \frac{\partial A_{sys,eq*}}{\partial K_{eq}} v \tag{24}$$

The second-order eigen-sensitivity is given by (25), where  $w$  is the left eigenvector,  $I$  is an identity matrix, and the superscript T denotes the transpose.

$$\frac{\partial^2 \lambda_i}{\partial K_{eq}^2} = 2w^T \left( \frac{\partial A_{sys,eq*}}{\partial K_{eq}} - \frac{\partial \lambda_i}{\partial K_{eq}} I \right) \frac{\partial v}{\partial K_{eq}} + w^T \frac{\partial^2 A_{sys,eq*}}{\partial K_{eq}^2} v \tag{25}$$

To solve (25), the sensitivity of the eigenvector ( $\partial v / \partial K_{eq}$ ) is required, derived as (26) and (27). However,  $(A_{sys,eq*} - \lambda_i I)$  is singular and (27) cannot be solved.

$$(A_{sys,eq*} - \lambda_i I) v = 0 \tag{26}$$

$$(A_{sys,eq*} - \lambda_i I) \frac{\partial v}{\partial K_{eq}} + \left( \frac{\partial A_{sys,eq*}}{\partial K_{eq}} - \frac{\partial \lambda_i}{\partial K_{eq}} I \right) v = 0 \tag{27}$$

Multiplying a complex number  $k \angle \theta$  to both sides of (26), one obtains (28). It can be found that the eigenvectors corresponding to different  $k$  and  $\theta$  satisfy (26). Hence, for each eigenvalue, there are numerous eigenvectors, as shown in Figure 5.

$$(A_{sys,eq*} - \lambda_i I) (vk \angle \theta) = 0 \tag{28}$$

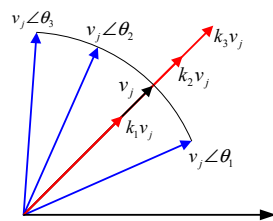


Figure 5. Multiple solutions of eigenvectors.

The red line in Figure 5 is the eigenvectors considering the effect of  $k$ , and the blue line is the eigenvectors after considering the  $\theta$ , which has directionality.

To find a unique eigenvector for eigen-sensitivity analysis, the constraints of the magnitude and angle of  $v_j$  are to be added, where  $C_1$  and  $C_2$  are the constants (29).

$$v_j = |v_j| \angle \theta_j = C_1 \angle C_2 \tag{29}$$

The normalization condition is derived in (30). Combining (27) and (30), the eigenvector sensitivity and the second-order eigenvalue sensitivity are found, which removes the obstacle to optimize  $K_{eq}$  for the SMC.

$$\frac{\partial v_j}{\partial K_{eq}} = 0 \Rightarrow \begin{cases} \frac{\partial |v_j|}{\partial K_{eq}} = 0 \\ \frac{\partial \theta_j}{\partial K_{eq}} = 0 \end{cases} \tag{30}$$

Then, the LFO mode  $\lambda_i$  and its damping ratio  $\xi_i$  are given by the first- and the second-order eigen-sensitivities

$$\lambda_i = \lambda_{i,0} + \frac{\partial \lambda_i}{\partial K_{eq}} K_{eq} + \frac{1}{2} \frac{\partial^2 \lambda_i}{\partial K_{eq}^2} K_{eq}^2 \tag{31}$$

$$\begin{aligned} \bar{\xi}_i = \xi_{i,0} + \mu_i \left( -\frac{\partial \sigma_i}{\partial K_{eq}} \mu_i + \sigma_i \frac{\partial \mu_i}{\partial K_{eq}} \right) \frac{1}{|\lambda_i|^3} K_{eq} \\ + \frac{1}{2|\lambda_i|^5} \left[ \begin{array}{l} 3\sigma_i \mu_i^2 \left( \frac{\partial \sigma_i}{\partial K_{eq}} \right)^2 + \sigma_i \left( |\lambda_i|^2 - 3\mu_i^2 \right) \left( \frac{\partial \mu_i}{\partial K_{eq}} \right)^2 \\ + \mu_i \left( -|\lambda_i|^2 + 3\mu_i^2 - 3\sigma_i^2 \right) \frac{\partial \sigma_i}{\partial K_{eq}} \frac{\partial \mu_i}{\partial K_{eq}} \\ \mu_i |\lambda_i|^2 \left( -\mu_i \frac{\partial^2 \sigma_i}{\partial K_{eq}^2} + \sigma_i \frac{\partial^2 \mu_i}{\partial K_{eq}^2} \right) \end{array} \right] K_{eq}^2 \end{aligned} \tag{32}$$

### 4.3. Framework of Eigen-Sensitivity-Based Second-Order SMC

The proposed eigen-sensitivity-based second-order SMC is given in Figure 6. It has four steps: (i) derive the state space model of the power system with the DFIG and find the critical LFO modes, (ii) design the sliding surface based on the states strongly associated with the critical mode, (iii) optimize  $K_{eq}$  based on the eigen-sensitivities to balance the damping effect on the critical mode and the undesirable effect on other modes, and (iv) design the switch control based on the super-twisting algorithm.

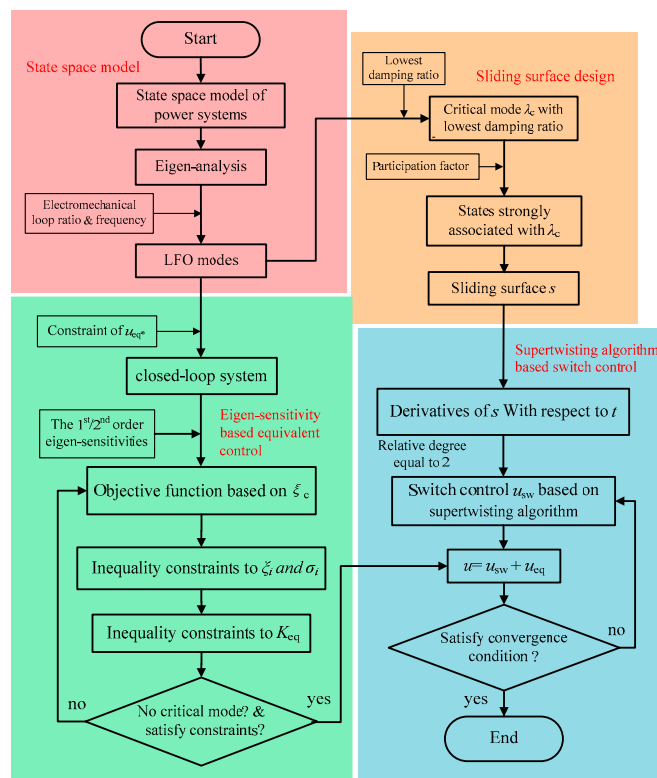


Figure 6. Eigen-sensitivity-based second-order SMC for LFO damping.

It should be noted that although the SMC is nonlinear, the above control is based on a linearized state space at a given initial point; hence, it is feasible for large systems. For the systems with high nonlinearity, uncertainty, or extremely large disturbance, the successive multi-step optimization may be applied.

The chattering phenomena of the SMC is a restriction of the proposed method. In future work, it is possible to consider how to improve the SMC law to suppress the chattering problem. In addition, the adaptive optimization of the  $K_{eq}$  at different operating

points of the power system makes the SMC more adaptive. The POD control effect is improved in the transient situation of the DFIG-integrated power system.

### 5. Case Study

The case studies are performed on the New England 39-bus system [54] (Figure 7). At bus 9, a wind farm with 90 DFIGs is aggregated to DFIG1. At bus 21, a wind farm with 40 DFIGs is aggregated to DFIG2. The wind speeds  $v_{w1}$  and  $v_{w2}$  of the two wind farms are 12 and 9 m/s, respectively. The parameters of a single DFIG are found in [49]. The criterion to find the critical model is  $\sigma_{lim} = -0.1$  and  $\zeta_{lim} = 0.02$ .

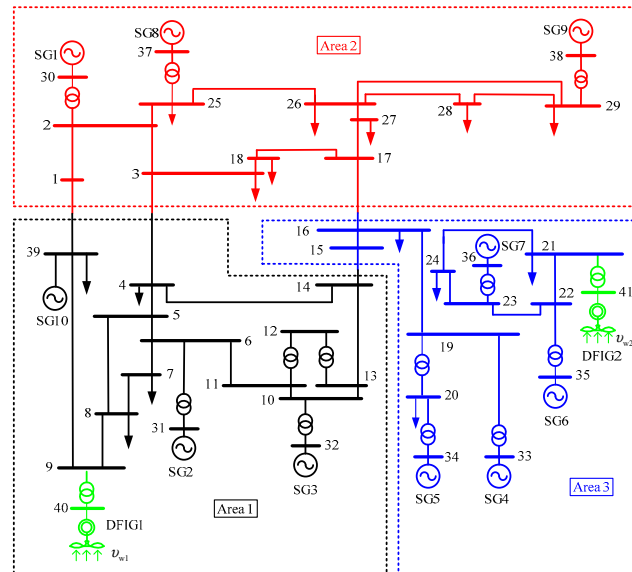


Figure 7. New England 39-bus system with DFIG-based wind farms.

#### 5.1. Deciding the Location of SMC Based on Eigen-Analysis

##### 5.1.1. Impact of DFIG on LFO

The LFO modes without/with the DFIGs are shown in Figure 8. Some modes change notably with the DFIG. Among the LFO modes,  $\lambda_{25,26}$  is considered as the critical mode due to the lowest damping ratio.  $\lambda$  is the eigenvalue of the power system.

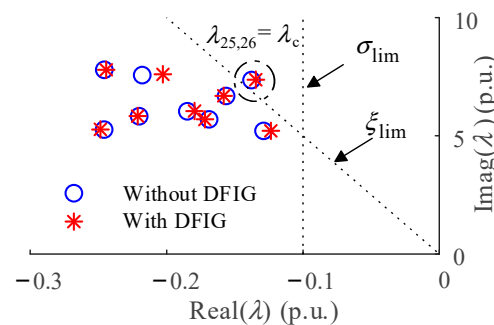


Figure 8. Impact of DFIG integration on the LFO modes.

##### 5.1.2. Selecting the Sliding Surface

Figure 9 shows the participation factor of the SGs to  $\lambda_{25,26}$ . It is found that SG1 and SG8 are most strongly associated with  $\lambda_{25,26}$ ; hence, the difference in their rotor speeds is selected to design the sliding surface, i.e.,  $s = \omega_1 - \omega_8 = \omega_{1,8}$ .

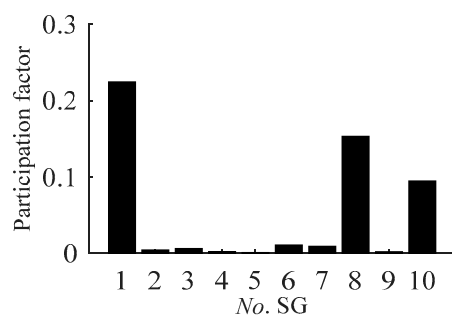


Figure 9. Participation factors to  $\lambda_{25,26}$ .

### 5.1.3. The Optimal Location of SMC

To decide the location of the SMC, the first-order sensitivities of  $\lambda_{25,26}$  with respect to the control parameters of the DFIGs' converters are calculated. With regulating  $P_s$ ,  $Q_s$ ,  $V_{dc}$ , or  $Q_g$ , noted as schemes a, b, c, and d, respectively, the largest value of the eigen-sensitivities corresponding to different control loops is shown in Figure 10. The eigen-sensitivity with the active power loop of the RSC of DFIG1 is the largest. Hence, the SMC is installed at the active power control loop of the RSC of DFIG1.

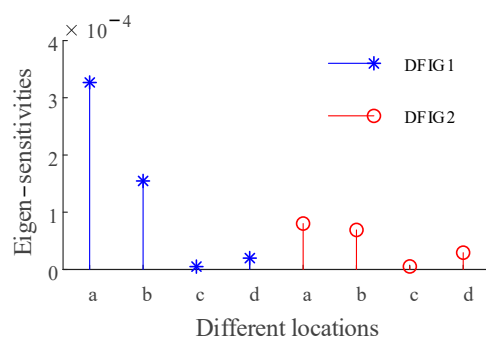


Figure 10. Eigen-sensitivity of  $\lambda_{25,26}$  to control parameters of converters.

## 5.2. Validation of Impact of Equivalent Control

### 5.2.1. Effect of Conventional Equivalent Control

The impact of the conventional equivalent control  $u_{eq}$  on the states is studied with the LFO modes of the power systems with and without  $u_{eq}$ . As seen in Table 1, the critical mode  $\lambda_{25,26}$  (in bold) strongly associated with the states of the sliding surface is improved. However, in addition to  $\lambda_{25,26}$ ,  $u_{eq}$  changes other modes. The damping ratio of  $\lambda_{30,31}$  (in bold) is now negative, which means the undesirable effect endangers the stability of the power systems.

Table 1. Undesirable Effect of Conventional Equivalent Control.

	Without $u_{eq}$		With $u_{eq}$	
	Eigenvalue (p.u.)	$\xi$	Eigenvalue (p.u.)	$\xi$
$\lambda_{21,22}$	$-0.244 \pm 7.794i$	0.0313	$-0.261 \pm 7.809i$	0.0334
$\lambda_{23,24}$	$-0.202 \pm 7.601i$	0.0267	$-0.135 \pm 7.778i$	0.0173
<b><math>\lambda_{25,26}</math></b>	<b><math>-0.136 \pm 7.374i</math></b>	0.0183	<b><math>-2.196 \pm 3.957i</math></b>	0.4852
$\lambda_{28,29}$	$-0.158 \pm 6.694i$	0.0236	$-0.162 \pm 6.690i$	0.0242
$\lambda_{30,31}$	$-0.180 \pm 6.050i$	0.0297	$1.097 \pm 4.662i$	<b>-0.2290</b>
$\lambda_{32,33}$	$-0.221 \pm 5.836i$	0.0379	$-0.240 \pm 5.847i$	0.0409
$\lambda_{34,35}$	$-0.172 \pm 5.697i$	0.0302	$-0.176 \pm 5.735i$	0.0307
$\lambda_{36,37}$	$-0.249 \pm 5.273i$	0.0471	$-0.289 \pm 5.244i$	0.0512
$\lambda_{38,39}$	$-0.124 \pm 5.210i$	0.0237	$-0.114 \pm 5.233i$	0.0217

5.2.2. Effect of Improved Equivalent Control

To avoid the undesirable effect, the improved equivalent control  $u_{eq}^*$  is applied. The locus of  $\lambda_{25,26}$  and  $\lambda_{30,31}$  and their damping ratio with different  $K_{eq}$  are studied to quantify the damping effect with  $u_{eq}^*$ , as shown in Figure 11. The  $\zeta$  is the damping ratio of the power system. A large  $K_{eq}$  helps to damp  $\lambda_{25,26}$ , but yields the negative damping mode of  $\lambda_{30,31}$ . Hence,  $K_{eq}$  may be optimized to improve the control effect.

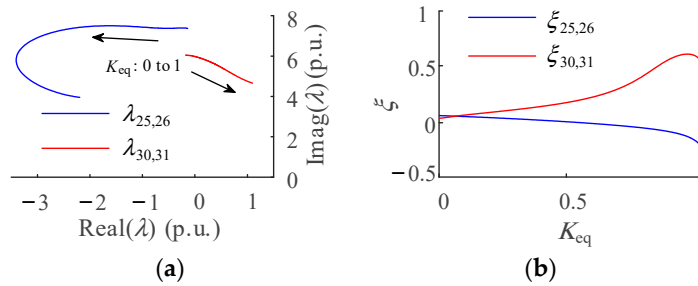


Figure 11. Impact of  $u_{eq}^*$  on LFOs. (a)  $\lambda_{25,26}$  and  $\lambda_{30,31}$ , (b)  $\zeta_{25,26}$  and  $\zeta_{30,31}$ .

The first- and second-order sensitivities of  $\lambda_{25,26}$  and  $\lambda_{30,31}$  with respect to  $K_{eq}$  are given in Table 2, providing information about the impact of  $u_{eq}^*$  on the states. The sign of  $\partial\zeta_{25,26}/\partial K_{eq}$  and  $\partial\zeta_{30,31}/\partial K_{eq}$  explains the different trends of  $\lambda_{25,26}$  and  $\lambda_{30,31}$  with the change in  $K_{eq}$ . The second-order eigenvalue sensitivity is quite large, which shows the non-linearity of the power systems, and adds the difficulty of robust control to the LFO modes.

Table 2. The first- and second-Order Sensitivities of LFO Modes.

	Eigen-Sensitivities (p.u.)		Eigen-Sensitivities (p.u.)	
$\partial\lambda_{25,26}/\partial K_{eq}$	$-1.6223 \pm 0.7648i$	$\partial\lambda_{30,31}/\partial K_{eq}$	$0.4455 \pm 0.0325i$	
$\partial^2\lambda_{25,26}/\partial K_{eq}^2$	$-3.7300 \pm 0.6762i$	$\partial^2\lambda_{30,31}/\partial K_{eq}^2$	$0.3393 \pm 1.3890i$	

Based on the first- and the second-order eigen-sensitivities,  $K_{eq}$  is optimized to design  $u_{eq}^*$ . With the constraints of  $\lambda_{30,31}$ , the undesirable effect is considered. The optimized  $K_{eq}$  is 0.117, and  $\lambda_{25,26}$  and  $\lambda_{30,31}$  are given in Table 3. At the expense of optimizing  $K_{eq}$ ,  $\zeta_{25,26}$  is less than that in Table 1, but  $\zeta_{30,31}$  satisfies  $\zeta_{lim}$ , showing that the constraint is effective to limit the undesirable effect.

Table 3. Control Effect with Optimized  $K_{eq}$ .

Mode	Value	Mode	Value
$\lambda_{25,26}$ (p.u.)	$-0.374 \pm 7.386i$	$\lambda_{30,31}$ (p.u.)	$-0.121 \pm 6.035i$
$\zeta_{25,26}$	0.0506	$\zeta_{30,31}$	0.0200

5.2.3. Validation of Damping Effect of the Proposed SMC

A 3-phase short fault at bus 1 occurs at 0.3 s and is cleared at 0.4 s. At first, the effect with the second-order eigen-sensitivity-based equivalent control  $u_{eq}^*$  on the sliding surface is verified. Then, the control effect of  $u_{eq}^*$  and the super-twisting algorithm-based switch control  $u_{sw}$  is verified.

At first, the equivalent control law is introduced. The rotor dynamics of SG1 and SG8, closely related to the sliding surface, are shown in Figure 12. Oscillations of  $\omega_{1,8}$  and  $\delta_{1,8}$  damped by  $u_{eq}$  (blue) and  $u_{eq}^*$  (red) are compared with those without  $u_{eq}$  (black). It can be seen that the negatively damped mode  $\lambda_{30,31}$  caused by  $u_{eq}$  yields the oscillation of  $\omega_{1,8}$  and instability of  $\delta_{1,8}$ , which is successfully avoided by using  $u_{eq}^*$ .  $\delta$  is the power angle of the SG.

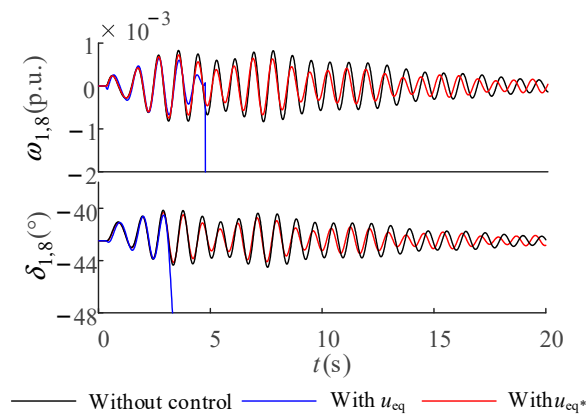


Figure 12. Control effect of  $u_{eq}$  and  $u_{eq}^*$  on the sliding surface.

Then,  $u_{sw}$  is applied independently, or together with  $u_{eq}^*$ . For scheme (a) without the SMC, (b) with  $u_{sw}$ , and (c) with  $u_{eq}^*$  and  $u_{sw}$ , the rotor dynamics are shown in Figure 13. Oscillations of  $\omega_{1,8}$  and  $\delta_{1,8}$  are damped with three schemes, but the attenuation time is different. With the criterion of 5% of the oscillation amplitude, the attenuation times of scheme (c), i.e., 20.58 s and 20.83 s, are much shorter, i.e.,  $u_{eq}^*$  accelerates the states reaching the sliding surface; hence, it improves the system’s stability.

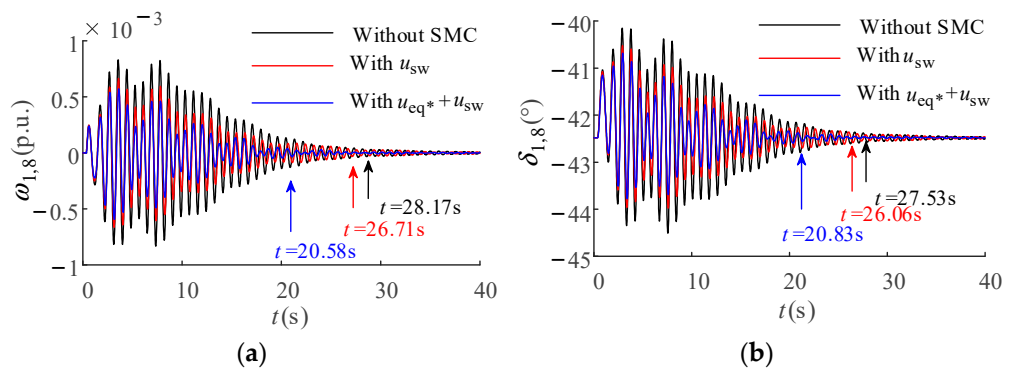


Figure 13. Attenuation time of the proposed SMC. (a)  $\omega_{1,8}$ , (b)  $\delta_{1,8}$ .

To validate the damping effect of the proposed SMC, the largest magnitudes of  $\omega_{1,8}$  and  $\delta_{1,8}$  are given in Table 4. It can be found that the oscillations are damped by the SMC with  $u_{sw}$  effectively. By adding  $u_{eq}^*$  in scheme (c), the magnitudes are decreased by 12.8% and 12.5%, respectively. The damping effect is more obvious.

Table 4. Damping Effect on SG with Proposed SMC.

	No SMC	$u_{sw}$	$u_{eq}^* + u_{sw}$
$\Delta\omega_{1,8}$ (p.u.)	$8.31 \times 10^{-4}$	$6.64 \times 10^{-4}$	$5.60 \times 10^{-4}$
$\Delta\delta_{1,8}$ (°)	2.33	2.06	1.76

### 5.3. Validation of Robustness of SMC

To validate the control effect of the proposed SMC in uncertain system conditions, the wind speed of DFIG1, varying from 9 m/s to 14 m/s, is given in Figure 14. The oscillations of  $\omega_{1,8}$  in Figure 15 show that the LFOs are damped by the proposed SMC effectively, which proves the robustness of the SMC against the variation in wind speeds.  $V_{w1}$  is the wind speed of DFIG1.

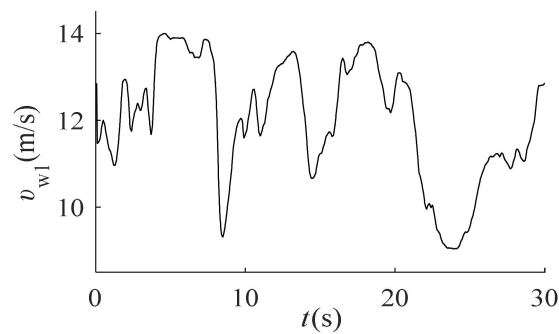


Figure 14. Wind speed change.

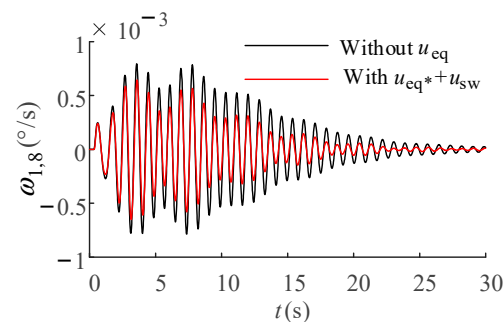


Figure 15. Control effect of SMC with changing speeds.

## 6. Conclusions

This paper studies the LFO damping of the SGs in wind power systems. The state equations of the system with the SGs and DFIGs are derived to find the critical modes. The states strongly associated with the critical modes are applied to select the sliding surface of the SMC. The equivalent control of the SMC is improved with a gain to avoid the undesirable effect on the noncritical modes. The optimization model of the gain with the objective of the damping ratio of the critical mode and the constraints of the noncritical modes is proposed and solved with the second-order eigen-sensitivity. The theoretical derivation and numerical results show that:

- (1) Using the existing SMC with the equivalent control, the damping ratio of noncritical modes may be decreased, which is avoided in this paper with the proposed improved equivalent control of the gain constrained by the optimization model.
- (2) The analytical model of the eigen-sensitivity is the basis to derive the optimization model for the gain. The eigenvector sensitivity is necessary to find the second-order eigen-sensitivity.
- (3) Compared with the existing SMC, the proposed SMC not only damps the LFO effectively, but also accelerates the states reaching the sliding surface; hence, it saves time for the LFO damping. It is robust with different wind speeds.

The main restriction in the proposed scheme is the chattering phenomena caused by the discontinuous control action when the operating system approaches the sliding manifold. The improved sliding mode control law to suppress the chattering problem is considered in future work. Since the LFOs are damped by the PSS at the SGs and the PODs at the high-voltage dc converter stations, the shunt or series compensators, the wind farms, and photovoltaic stations, in the following research, the dynamic interaction among these dampers may be included to optimize these parameters against uncertain system conditions and severe disturbances.

**Author Contributions:** Conceptualization, reviewing, and funding acquisition: S.L., R.Z., H.Z. and J.Y. Modeling, simulation, writing—original draft preparation and editing, resources and software, and data curation: S.L., H.Z., J.Y., R.Z., J.W. and Q.L. All authors have read and agreed to the published version of the manuscript.

**Funding:** This research was funded by State Grid Anhui Electric Power Co. Ltd. Program under grant 52120022000B.

**Data Availability Statement:** Not applicable.

**Conflicts of Interest:** The authors declare no conflict of interest.

## Nomenclature

### Abbreviations

DFIG	Doubly fed induction generator.
GSC, RSC	Grid/rotor-side converter.
LFO	Low-frequency oscillation.
PAC	Pitch angle control.
POD	Power oscillation damper.
PSS	Power system stabilizer.
SG	Synchronous generator.
SMC	Sliding mode control.
WT	Wind turbine.

### Notations

$A, B, C, D, E, F$	Coefficient matrices.
$A_{\text{sys}}$	State matrix of power systems.
$F$	Objective function.
$I$	Identity matrix.
$L, o, q$	Lagrange function, Lagrange multipliers.
$p$	Participation factor.
$s, u$	Sliding surface, control signal of the SMC.
$V, I, Y$	Voltage, current, and admittance matrix
$w, v$	Left/right eigenvector.
$x, y$	State/algebraic variable.
$v_w$	Wind speed.
$\omega, f$	Rotor speed and frequency.
$\delta$	Power angle.
$\rho$	Electromechanical loop participation ratio.
$\lambda, \zeta$	Eigenvalue and damping ratio.
$\sigma, \mu$	Real/imaginary part of eigenvalues.
$\kappa, l$	Slack variables.
$\Delta$	Deviation of variables.
$N$	Number of state variables
$M$	Number of algebraic variables

### Subscripts

c	Critical mode.
eq	Equivalent control.
eq*	Improved equivalent control.
sw	Switch control.
s, r	Stator and rotor.
d, q	Direct/quadrature axis.
MT	Mechanical transient.
T	Transmission system.
t	Transfer shaft.
0	Initial value.
lim	Marginal value.

### Superscripts

min, max	Minimum/maximum value.
*	Reference value.

## References

1. Abdalzaher, M.S.; Fouda, M.M.; Ibrahim, M.I. Data privacy preservation and security in smart metering systems. *Energies* **2022**, *15*, 7419. [[CrossRef](#)]
2. Abdalzaher, M.S.; Fouda, M.M.; Emran, A.; Fadlullah, Z.M.; Ibrahim, M.I. A survey on key management and authentication approaches in smart metering systems. *Energies* **2023**, *16*, 2355. [[CrossRef](#)]
3. Wu, Z.; Li, S. Reliability evaluation and sensitivity analysis to AC/UHVDC systems based on sequential Monte Carlo simulation. *IEEE Trans. Power Syst.* **2019**, *34*, 3156–3167. [[CrossRef](#)]
4. Li, S.; Dong, W. Wind power system reliability sensitivity analysis by considering forecast error based on non-standard third-order polynomial normal transformation method. *Electr. Power Syst. Res.* **2019**, *167*, 122–129. [[CrossRef](#)]
5. Li, S.; Zhang, H. Improved eigen-sensitivity with respect to transfer function of DFIG-PSS in wind power systems. *Electr. Power Compon. Syst.* **2021**, *48*, 1735–1746.
6. Du, W.; Chen, X.; Wang, H. DFIG oscillation modes causing strong dynamic interactions to degrade the damping of power system low-frequency electromechanical oscillations. *Electr. Power Compon. Syst.* **2019**, *47*, 288–300. [[CrossRef](#)]
7. Yu, Y.; Min, Y.; Grijalva, S.; Thomas, J.J.; Xiong, L.; Ju, P.; Min, Y. Oscillation energy analysis of inter-area low-frequency oscillations in power systems. *IEEE Trans. Power Syst.* **2016**, *31*, 1195–1203. [[CrossRef](#)]
8. Wang, Z.; Shen, C.; Liu, F. Probabilistic analysis of small signal stability for power systems with high penetration of wind generation. *IEEE Trans. Sustain Energy* **2016**, *7*, 1182–1193. [[CrossRef](#)]
9. Ma, J.; Zhang, Y.; Shen, Y. Equipment-level locating of low frequency oscillating source in power system with DFIG integration based on dynamic energy flow. *IEEE Trans. Power Syst.* **2020**, *35*, 3433–3447. [[CrossRef](#)]
10. Gupta, A.K.; Verma, K.; Niazi, K.R. Dynamic impact analysis of DFIG-based wind turbine generators on low-frequency oscillations in power system. *IET Gener. Transm. Dis.* **2017**, *11*, 4500–4510. [[CrossRef](#)]
11. Kayikci, M.; Milanovic, J.V. Dynamic contribution of DFIG-based wind plants to system frequency disturbances. *IEEE Trans. Power Syst.* **2009**, *24*, 859–867. [[CrossRef](#)]
12. Chaudhuri, N.R.; Chaudhuri, B. Considerations toward coordinated control of DFIG-based wind farms. *IEEE Trans. Power Deliv.* **2013**, *28*, 1263–1270. [[CrossRef](#)]
13. Isbeih, Y.J.; Moursi, M.S.E.  $H_{\infty}$  mixed-sensitivity robust control design for damping low-frequency oscillations with DFIG wind power generation. *IET Gener. Transm. Dis.* **2019**, *13*, 4274–4286. [[CrossRef](#)]
14. Jawaharlal, B.; Vasundhara, M. Mathematical modelling and stability analysis of PSS for damping LFOs of wind power system. *IET Renew. Power Gener.* **2019**, *13*, 103–115.
15. Fan, L.; Yin, H.; Miao, Z. On active/reactive power modulation of DFIG-based wind generation for interarea oscillation damping. *IEEE Trans. Energy Convers.* **2011**, *26*, 513–521.
16. Ajit, K. Power system stabilizers design for multimachine power systems using local measurements. *IEEE Trans. Power Syst.* **2016**, *31*, 2163–2171.
17. Du, W.; Dong, W.; Wang, Y.; Wang, H. A method to design power system stabilizers in a multi-machine power system based on single-machine infinite-bus system model. *IEEE Trans. Power Syst.* **2021**, *36*, 3457–3586. [[CrossRef](#)]
18. Elazim, S.M.A.; Ali, E.S. Optimal SSSC Design for Damping Power Systems Oscillations via Gravitational Search Algorithm. *Int. J. Power Energy Syst.* **2016**, *82*, 161–168. [[CrossRef](#)]
19. Abd-Elazim, S.M.; Ali, E.S. Imperialist competitive algorithm for optimal STATCOM design in a multimachine power system. *Int. J. Power Energy Syst.* **2016**, *76*, 136–146. [[CrossRef](#)]
20. Abd-Elazim, S.M.; Ali, E.S. Coordinated design of PSSs and SVC via bacteria foraging optimization algorithm in a multimachine power system. *Int. J. Power Energy Syst.* **2012**, *41*, 44–53. [[CrossRef](#)]
21. Ali, E.S.; Abd-Elazim, S.M. Coordinated design of PSSs and TCSC via bacterial swarm optimization algorithm in a multimachine power system. *Int. J. Power Energy Syst.* **2012**, *36*, 84–92. [[CrossRef](#)]
22. Gibbard, M.J.; Vowles, D.J. Reconciliation of methods of compensation for PSSs in multimachine systems. *IEEE Trans. Power Syst.* **2004**, *19*, 463–472. [[CrossRef](#)]
23. Wang, L.; Chang, C.; Kuan, B.; Prokhorov, A.V. Stability improvement of a two-area power system connected with an integrated onshore and offshore wind farm using a STATCOM. *IEEE Trans. Ind. Appl.* **2017**, *53*, 867–877. [[CrossRef](#)]
24. Sun, L.; Liu, K.; Hu, J.; Hou, Y. Analysis and mitigation of electromechanical oscillations for DFIG wind turbines involved in fast frequency response. *IEEE Trans. Power Syst.* **2019**, *34*, 4547–4556. [[CrossRef](#)]
25. Jalayer, R.; Ooi, B.T. Coordinated PSS tuning of large power systems by combining transfer function-eigenfunction analysis (TFEA), optimization, and eigenvalue sensitivity. *IEEE Trans. Power Syst.* **2014**, *29*, 2672–2680. [[CrossRef](#)]
26. Li, S.; Zhang, H.; Kai, Y. Optimization to POD parameters of DFIGs based on the 2nd order eigenvalue sensitivity of power systems. *IET Gener. Transm. Dis.* **2021**, *15*, 1123–1135. [[CrossRef](#)]
27. Ma, J.; Ma, X.; Hill, D.; Zhao, D.; Zhu, L.; Chi, Y. Developing feedback model for power system dynamic sensitivity analysis. *Int. Trans. Electr. Energy Syst.* **2017**, *27*, 1–14. [[CrossRef](#)]
28. Li, S. Low-frequency oscillations of wind power systems caused by doubly-fed induction generators. *Renew. Energy* **2017**, *104*, 129–138. [[CrossRef](#)]
29. Juang, C.; Lu, C. Load-frequency control by hybrid evolutionary fuzzy PI controller. *IEE Proc. Gener. Transm. Dis.* **2006**, *153*, 196–204. [[CrossRef](#)]

30. Wu, B.; Malik, O.P. Multivariable adaptive control of synchronous machines in a multimachine power system. *IEEE Trans. Power Syst.* **2006**, *21*, 1772–1781. [[CrossRef](#)]
31. Wang, L.; Yang, R.; Zhang, H. Improved event-triggered sliding mode control of switched systems with disturbances. *Asian J. Control.* **2021**, *23*, 2214–2226. [[CrossRef](#)]
32. Mi, Y.; Hao, X.; Liu, Y.; Fu, Y.; Wang, C.; Wang, P.; Loh, P.C. Sliding mode load frequency control for multiarea time-delay power system with wind power integration. *IET Gener. Transm. Dis.* **2017**, *11*, 4644–4653. [[CrossRef](#)]
33. Saoudi, K.; Harmas, M.N. Enhanced design of an indirect adaptive fuzzy sliding mode power system stabilizer for multi-machine power systems. *Int. J. Electr. Power Energy Syst.* **2014**, *54*, 425–431. [[CrossRef](#)]
34. Liao, K.; He, Z.; Xu, Y.; Chen, G.; Dong, Z.; Wong, K. A sliding mode based damping control of DFIG for interarea power oscillations. *IEEE Trans. Sustain. Energy* **2017**, *8*, 258–267. [[CrossRef](#)]
35. Liao, K.; Xu, Y. A robust load frequency control scheme for power systems based on second-order sliding mode and extended disturbance observer. *IEEE Trans. Industr. Inform.* **2018**, *14*, 3076–3086. [[CrossRef](#)]
36. Ahmad, J.; Ghazanfar, S. Analysis and simulation of a sliding mode controller for mechanical part of a doubly-fed induction generator-based wind turbine. *IET Gener. Transm. Dis.* **2017**, *11*, 2677–2688.
37. Mi, Y.; Fu, Y.; Wang, C.; Wang, P. Decentralized sliding mode load frequency control for multi-area power systems. *IEEE Trans. Power Syst.* **2013**, *28*, 4301–4309. [[CrossRef](#)]
38. Arie, L. Principles of 2-sliding mode design. *Automatica* **2007**, *43*, 576–586.
39. Mi, Y.; He, X.; Hao, X.; Li, Z.; Fu, Y.; Wang, C.; Wang, J. Frequency control strategy of multi-area hybrid power system based on frequency division and sliding mode algorithm. *IET Gener. Transm. Dis.* **2019**, *13*, 1145–1152. [[CrossRef](#)]
40. Chung, S.C.; Lin, C.L. A general class of sliding surface for sliding mode control. *IEEE Trans. Automat. Control.* **1998**, *43*, 115–119. [[CrossRef](#)]
41. Zhang, X.; Su, H.; Lu, R. Second-order integral sliding mode control for uncertain systems with control input time delay based on singular perturbation approach. *IEEE Trans. Automat. Control.* **2015**, *60*, 3095–3100. [[CrossRef](#)]
42. Yu, H.; Liu, T.S. Sliding mode control using virtual eigenvalue method for compact optical image stabilization actuators. *IEEE Trans. Magn.* **2008**, *44*, 4074–4077.
43. Tang, C.Y.; Misawa, E.A. Sliding surface design for a discrete VSS using LQR technique with a preset eigenvalue. In Proceedings of the American Control Conference, San Diego, CA, USA, 2–4 June 1999; pp. 520–524.
44. Janardhanan, S.; Kariwala, V. Multirate-output-feedback-based LQ-optimal discrete-time sliding mode control. *IEEE Trans. Control Syst. Technol.* **2008**, *53*, 367–373. [[CrossRef](#)]
45. Silva, J.M.A.-D.; Edwards, C.; Spurgeon, S.K. Sliding-mode output-feedback control based on LMIs for plants with mismatched uncertainties. *IEEE Trans. Ind. Electron.* **2009**, *56*, 3675–3683. [[CrossRef](#)]
46. Gupta, A.K.; Verma, K.; Niazi, K.R. Wide area coordinated control for low-frequency oscillations damping in a wind-integrated power system. *J. Eng.* **2019**, *18*, 4941–4945. [[CrossRef](#)]
47. Yan, C.; Yan, W.; Wen, J.; Fang, J.; Ai, X. Optimal design of probabilistic robust damping controllers to suppress multiband oscillations of power systems integrated with wind farm. *Renew. Energ.* **2020**, *158*, 75–90. [[CrossRef](#)]
48. Li, S.; Fang, T.; Zhang, H.; Ye, J. Damping the electromechanical oscillation modes (EOMs) in DFIG-integrated power systems with sensitivity analysis and optimization to outputs of SGs. *Int. J. Electr. Power Energy Syst.* **2022**, *135*, 107565. [[CrossRef](#)]
49. Li, S.; Huang, J.; Zhang, H.; Li, Z. Successive linear programming to improve small-signal stability of power systems with doubly-fed induction generators. *Electr. Power Compon. Syst.* **2019**, *47*, 927–939. [[CrossRef](#)]
50. Li, S.; Zhang, H.; Yan, Y.; Ren, J. Parameter optimization to power oscillation damper (POD) considering its impact on the DFIG. *IEEE Trans. Power Syst.* **2022**, *37*, 1508–1518. [[CrossRef](#)]
51. Ma, J.; Wang, S.; Li, Y.; Qiu, Y. Power system multi-parameter small signal stability analysis based on 2nd order perturbation theory. *Int. J. Electr. Power Energy Syst.* **2015**, *67*, 409–416. [[CrossRef](#)]
52. Wang, K.; Chuang, C.; Tse, C.T.; Tsang, K.M. Multimachine eigenvalue sensitivities of power system parameters. *IEEE Trans. Power Syst.* **2020**, *15*, 741–747. [[CrossRef](#)]
53. Condren, J.; Gedra, T.W. Expected-security-cost optimal power flow with small-signal stability constraints. *IEEE Trans. Power Syst.* **2006**, *21*, 1736–1743. [[CrossRef](#)]
54. Li, J.; Chen, Z.; Cai, D.; Zhen, W.; Huang, Q. Delay-dependent stability control for power system with multiple time-delays. *IEEE Trans. Power Syst.* **2016**, *31*, 2316–2326. [[CrossRef](#)]

**Disclaimer/Publisher’s Note:** The statements, opinions and data contained in all publications are solely those of the individual author(s) and contributor(s) and not of MDPI and/or the editor(s). MDPI and/or the editor(s) disclaim responsibility for any injury to people or property resulting from any ideas, methods, instructions or products referred to in the content.